

# NGC 6240 Supermassive Black Hole Binary dynamical evolution based on *Chandra* data

M. Sobolenko<sup>1</sup>,<sup>\*</sup> O. Kompaniiets<sup>1,2</sup>, P. Berczik<sup>3,4,1</sup>, V. Marchenko<sup>5</sup>, A. Vasylenko<sup>1</sup>,  
E. Fedorova<sup>6,7,8</sup>, B. Shukirgaliyev<sup>9,10,11</sup>

<sup>1</sup>Main Astronomical Observatory, National Academy of Sciences of Ukraine, 27 Akademika Zabolotnoho St, 03143 Kyiv, Ukraine

<sup>2</sup>Institute of Physics, National Academy of Sciences of Ukraine, 46 av. Nauky, 03028 Kyiv, Ukraine

<sup>3</sup>Astronomisches Rechen-Institut, Zentrum für Astronomie, University of Heidelberg, Mönchhofstrasse 12-14, 69120 Heidelberg, Germany

<sup>4</sup>Konkoly Observatory, Research Centre for Astronomy and Earth Sciences, Eötvös Loránd Research Network (ELKH),

MTA Centre of Excellence, Konkoly Thege Miklós út 15-17, 1121 Budapest, Hungary

<sup>5</sup>Astronomical Observatory, Jagiellonian University, 171 ul. Orła, 30-244 Krakow, Poland

<sup>6</sup>Astronomical Observatory, National Taras Shevchenko University of Kyiv, 3 Observatorna str., 04053 Kyiv, Ukraine

<sup>7</sup>INAF-Osservatorio Astronomico di Roma, via Frascati 33, I-00078 Monte Porzio Catone, Italy

<sup>8</sup>INAF-Osservatorio Astrofisico di Catania, Università di Catania, 95123 Catania, Italy

<sup>9</sup>Energetic Cosmos Laboratory, Nazarbayev University, 53 Kabanbay Batyr ave, 010000 Nur-Sultan, Kazakhstan

<sup>10</sup>Fesenkov Astrophysical Institute, 23 Observatory str, 050020 Almaty, Kazakhstan

<sup>11</sup>Al-Farabi Kazakh National University, 71 Al-Farabi ave, 050020 Almaty, Kazakhstan

Accepted XXX. Received YYY; in original form ZZZ

## ABSTRACT

The main idea of our research is to estimate the physical coalescence time of the double supermassive black hole (SMBH) system in the centre of NGC 6240 based on the X-ray observations from the *Chandra* space observatory. The spectra of the Northern and Southern nuclei were fitted by spectral models from Sherpa and both presented the narrow component of the Fe  $K\alpha$  emission line. It enabled us to apply the spectral model to these lines and to find relative offset  $\approx 0.02$  keV. The enclosed dynamical mass of the central region of NGC 6240 with radius 1 kpc was estimated  $\approx 2.04 \times 10^{11} M_{\odot}$ . These data allowed us to carry on the high resolution direct N-body simulations with Newtonian and post-Newtonian (up to  $2.5\mathcal{P}\mathcal{N}$  correction) dynamics for this particular double SMBH system. As a result, from our numerical models we approximated the central SMBH binary merging time for the different binary eccentricities. In our numerical parameters range the upper limit for the merging time, even for the very small eccentricities, is still below  $\approx 70$  Myr. Gravitational waveforms and amplitude-frequency pictures from such events can be detected using Pulsar Timing Array (PTA) projects at the last merging phase.

**Key words:** galaxies: active – galaxies: kinematics and dynamics – galaxies: individual: NGC6240 – X-rays: galaxies – black hole physics – gravitational waves

## 1 INTRODUCTION

The model of hierarchical galaxy evolution predicts galactic mergers (White & Rees 1978; Blumenthal et al. 1984; Kauffmann et al. 1999; Menci et al. 2002; Dobrycheva et al. 2018; Zoldan et al. 2019). Since the most observed galactic nuclei harbour the supermassive black holes (SMBHs) in their centre (Richstone et al. 1998; Ferrarese & Merritt 2000; Barausse 2012; Vavilova et al. 2015), the mergers of galaxies nearly always lead to the formation of the binary system of corresponding central SMBHs (Kormendy & Richstone 1995). Their evolution in the interacting galaxies can be described by three basic stages (Begelman et al. 1980).

In gas-free (dry merging) system the SMBHs become gravitational bound and create SMBH binary (SMBHB) when the semimajor axis approximately equals SMBHB influence radius. It is a sphere radius

that contains within the stellar mass equal to double black hole (BH) mass. The duration of this stage depends on the efficiency of the dynamical friction, but the system definitely forms a pc-scale SMBHB. Afterwards, the SMBHB separation shrinks due to the combined effect of dynamical friction and gravitational slingshot. When the latter process becomes dominating the binary reaches the hardening phase with a semimajor axis (Quinlan 1996; Yu 2002):

$$a_h \equiv \frac{G\mu}{4\sigma_*^2}, \quad (1)$$

where  $G$  is the gravitational constant, the binary reduced mass is  $\mu = M_{\text{BH1}}M_{\text{BH2}}/(M_{\text{BH1}} + M_{\text{BH2}})$  with primary and secondary BHs' masses  $M_{\text{BH1}}$  and  $M_{\text{BH2}}$  respectively, and  $\sigma_*$  is the velocity dispersion. The last merging stage is starting as the rapid coalescence of SMBHB via emission of gravitation waves (GWs) (Peters & Mathews 1963; Peters 1964a,b; Haehnelt 1994; Milosavljević & Merritt 2003a; Wyithe & Loeb 2003). After coalescence, a single formed SMBH is kicked from the merger remnant

\* Contact e-mail: sobolenko@mao.kiev.ua

centre and is observed as recoiling SMBH (Campanelli et al. 2007; Choi et al. 2007; González et al. 2007). The accompanying emission of GWs is equivalently taking away up to the 10 per cent of total rest-mass of binary system (Reisswig et al. 2009).

SMBHB evolution can be stalled between hardening and GW phases due to depletion of loss cone and merging time is becoming above Hubble time. The so-called ‘final parsec’ problem (Milosavljević & Merritt 2003b) occurs for idealised systems and can be solved in numerical simulations using the self-consistent equilibrium axisymmetric galaxy model (Berczik et al. 2006; Preto et al. 2011), using particles that have multiple encounters with central BHs (Avramov et al. 2021) or using massive perturbers in loss cone (Perets et al. 2007). Also, the presence of gas in interacting systems (wet merging) plays a significant but unpredictable role, that can decrease or increase the SMBHB merging time depending on system parameters (Cuadra et al. 2009; Lodato et al. 2009; Maureira-Fredes et al. 2018, for recent studies of gas and stars co-influence see Bortolas et al. 2021).

The natural way to search for such SMBHs is by looking at dual or binary active galactic nuclei (AGNs) (Husemann et al. 2020). Except for SMBH, the AGN also contains major components such as the accretion disk around the BH and molecular torus (e.g. Ricci et al. 2014; Vasylenko 2018; Gröbner et al. 2020; Kompaniits & Vasylenko 2020). Accretion onto SMBH is accompanied by converting the gravitational potential energy to the observed radiation, spanning the entire electromagnetic spectrum. Most of this energy dissipates in the innermost few gravitational radii leading to the bright X-ray emission.

X-ray radiation of AGN commonly is explained by thermal Comptonization of the soft ultraviolet (UV) radiation, produced by the inner parts of the accretion disk in a medium of ‘hot’ electrons around SMBH known as the corona (Haardt & Maraschi 1991, 1993). This radiation (called the primary emission) typically is described by a power-law model and an exponential cut-off at high energies where emission quickly roll-overs (Rybicki & Lightman 1979). Additionally to the continuum is specified the important reflected component, which is the reprocessed primary emission by a cold neutral circumnuclear medium (molecular torus or outer regions of the accretion disk). It is observed as a ‘reflection hump’ at  $\sim 20\text{--}30$  keV and emission in Fe  $K\alpha$  line at around 6.4 keV (e.g. Matt et al. 1991; Mushotzky et al. 1993). Due to a combination of abundances and fluorescent yield, the neutral Fe  $K\alpha$  at 6.4 keV is typically the strongest emission line seen in AGN’s X-ray spectra. If we found the energy difference for the observed Fe  $K\alpha$  lines we can assume that this shift is due to relative motion between two nuclei at the late stage. That gives the possibility to estimate the mass, enclosed within the common orbit of the binary system (i.e., dynamical mass).

One of the most prominent dual AGN candidates is nearby ultraluminous infrared galaxy (ULIRG) NGC 6240 ( $z = 0.0243$ ,  $D_L = 111.2$  Mpc<sup>1</sup>) that contains two heavily obscured Compton-thick nuclei separated by  $\sim 1''8$  (Gerssen et al. 2004). Multiple multiwavelength observations unfold complex morphological structure and confirm that it is in an active merging state (Pasquali et al. 2003). Clearly visible by *Hubble Space Telescope* (*HST*) irregular elongated morphology of this galaxy is often referred as ‘butterfly’ or ‘lobster-shaped’ (Müller-Sánchez et al. 2018). NGC 6240 is observed as the AGN in X-ray (Komossa et al. 2003; Puccetti et al. 2016; Fabbiano et al. 2020). It shows intensive starburst activity (Barger et al. 1998), supernova explosions of young hot stars

(Pignata et al. 2010) and contains H<sub>2</sub>O maser (Hagiwara et al. 2002, 2003). Another interesting property of this galaxy is the presence of the significant amount of dust surrounding the nucleus that causes its high infrared (IR) luminosity ( $\sim 10^{12} L_\odot$ ; see Sanders et al. 2003; Iono et al. 2007)<sup>2</sup>. The Multi-Element Radio Linked Interferometer Network (MERLIN) observations at 1.4 Ghz and 5 Ghz revealed two compact radio sources in the nuclei of NGC 6240 (Beswick et al. 2001). Followed-up high-resolution observations using Very Long Baseline Array (VLBA) and Very Long Baseline Interferometry (VLBI) detected a more complex structure of the central region with several radio sources. Two of the radio sources, namely N1 (Northern nucleus, further N) and S (or N2, Southern nucleus), matched with compact X-ray sources. The N nucleus may be clearly classified as AGN according to the characteristics in the radio band. The S nucleus spectrum contains composite emission from the AGN and circumnuclear starburst/supernova remnants (Gallimore & Beswick 2004; Hagiwara et al. 2011). Recently, the results by Kollatschny et al. (2020) and Fabbiano et al. (2020) about the double structure of the S-nucleus are under discussion.

The SMBH mass of the S nucleus lies in the range  $(0.87 - 2.0) \times 10^9 M_\odot$  obtained from the high resolution stellar kinematic results (Medling et al. 2011). Using *K*-band data from Very Large Telescope (VLT) and classical  $M_{\text{BH}}-\sigma$  relation (Tremaine et al. 2002), the N and S nucleus SMBH masses were estimated as  $(1.4 \pm 0.4) \times 10^8 M_\odot$  and  $(2.0 \pm 0.4) \times 10^8 M_\odot$ , respectively (Engel et al. 2010). Later, Treister et al. (2020) noticed that used by Engel et al. (2010) motion of the molecular gas, traced by the CO emission, rather aligns to the turbulence motion than to the circular movements. Recently obtained with MUSE instrument velocity dispersions correspond to N nucleus BH mass  $(3.6 \pm 0.8) \times 10^8 M_\odot$  and combined S (S1+S2) nucleus BH mass  $(8.0 \pm 0.8) \times 10^8 M_\odot$  (Kollatschny et al. 2020).

In the current work, we study the dynamical evolution of the SMBHB system in NGC 6240 using fully parallelised direct N-body code  $\varphi$ -GPU (Berczik et al. 2011). This evolution has been examined by performing several simulations of the two SMBHs dynamics, each of which is surrounded by its own bound stellar systems. These simulations required the initial parameters of the binary nucleus in the NGC 6240, which were obtained from spectral analysis of archival *Chandra* observations.

The paper is organised as follows. In Section 2 we present the analysis of X-ray emission from nuclei and dynamical mass estimation. Working code and relativistic treatment of the binary particles are described in Section 3. In Section 4 we describe a physical model and the set of numerical models for the NGC 6240 system based on our BH mass estimation. We applied our results to find the merging time for SMBHB and the expected GWs waveforms from this event in Section 5. Our conclusions are given in Section 6. Throughout this paper we assume  $\Lambda$ CDM cosmology with a Hubble constant of  $H_0 = 70$  km s<sup>-1</sup> Mpc<sup>-1</sup>,  $\Omega_M = 0.27$  and  $\Omega_\Lambda = 0.73$  (Bennett et al. 2003), which gives a scale  $1'' = 490$  pc (Wright 2006).

## 2 CHANDRA DATA ANALYSIS

### 2.1 Image and spectral analysis

NGC 6240 was observed by *Chandra* four times by Advanced CCD Imaging Spectrometer (ACIS) and once by High Resolution Camera (HRC). In the present work, we used only ACIS observations (ObsID 1590, 6908, 6909, 12713) with a total effective exposure

<sup>1</sup> <https://ned.ipac.caltech.edu/>

<sup>2</sup>  $L_{\text{IR}}$  is the 8–100  $\mu\text{m}$  luminosity



**Figure 1.** The *Chandra* images of NGC 6240 with the binning factor of 0.5: (left) the original merged image, (middle) the deconvolved image, (right) the exposure-corrected three-colour image, where colours correspond to energies: red: 0.5–2.5 keV, green: 2.5–6.0 keV, blue: 6.0–7.5 keV. The yellow line on the right panel is 5 kpc long.

time of 480.3 ks. The analysis of *Chandra* data was done with the CIAO 4.12 software package (Fruscione et al. 2006) and the calibration database CALDB 4.9.1. Before the analysis, the data were reprocessed using the `chandra_repro` script recommended in the CIAO analysis threads.

Firstly, the *Chandra* images in different energy bands (0.5–2.5 keV, 2.5–6.0 keV and 6.0–7.5 keV) were studied for carefully extracting the spectra from the regions corresponding to central BHs. We combined four ACIS observations using the `merge_obs` script from CIAO software package and created the exposure-corrected image (Fig. 1, right). It shows that the neutral Fe  $K\alpha$  emission lines were produced only in the central region of the galaxy which accords with the results presented by Komossa et al. (2003).

We restored the image to analyse the detailed spatial structure since the original X-ray data are degraded by the blurring function. To restore the image we applied the Lucy–Richardson Deconvolution Algorithm (LRDA) implemented in the CIAO tool `arestore`. This algorithm requires an image of Point Spread Function (PSF) which was modelled by the `ChART` and `MARX` programs for detailed ray-trace simulations (Carter et al. 2003; Wise 1997) (Fig. 1, left and middle). Consequently, we simulated the PSF for energy  $E = 6.25$  keV since we were interested mostly in the analysis of the central part of the galaxy where the emission is dominated by Fe  $K\alpha$  line. Two separate nuclei are more clearly visible due to the deconvolution (Fig. 1, middle). Furthermore, the galaxy butterfly-shape in X-ray band matches optical with O III cone, H $\alpha$  bubble, H $\alpha$  filaments and O III+H $\alpha$  filaments, which are a consequence of galaxies merging history (Müller-Sánchez et al. 2018).

The spectra were extracted from circular regions centred at the centroid position of two bright sources in the galaxy nuclei. The each radius was determined as  $3\sigma$  encircled count fraction regions of the correspondent PSFs that were separately modelled for the S and N nuclei. The sum of these regions’ diameters is  $2'' (\approx 1$  kpc) and can be taken as the maximum separation between the nuclei.

For the spectral analysis, we extracted the corresponding spectra from each ObsID using the `specextract` tool from the CIAO software package. The background spectrum was created for a circular region located outside the galaxy and subtracted from nuclei spectra. To take into account the telescope response we created the Auxiliary Response Files (ARF) and the Redistribution Matrix Files (RMF) separately for each ObsID. The spectra of the four ACIS observations for each region were combined using the `combine_spectra` script from

**Table 1.** The best-fitting parameters for X-ray spectra from Northern (N) and Southern (S) nuclei.

Parameter	N	S	Unit
Galactic absorption	0.0626 <sup>f</sup>	0.0626 <sup>f</sup>	10 <sup>22</sup> cm <sup>-2</sup>
Photon index $\Gamma$	1.75 <sup>f</sup>	1.75 <sup>f</sup>	
Absorbing column density $N_{\text{H}}$	5.00 <sup>+0.23</sup> <sub>-peg</sub>	31.30 <sup>+2.40</sup> <sub>-2.70</sub>	10 <sup>22</sup> cm <sup>-2</sup>
Line centre energy Fe $K\alpha$	6.41 <sup>+0.01</sup> <sub>-0.02</sub>	6.39 <sup>+0.01</sup> <sub>-0.02</sub>	keV
Line width $\sigma_{\text{Fe } K\alpha}$	0.05 <sup>+0.01</sup> <sub>-0.02</sub>	0.05 <sup>+0.04</sup> <sub>-0.03</sub>	keV
Line centre energy Fe xxv	6.72 <sup>+0.06</sup> <sub>-0.05</sub>	6.66 <sup>+0.06</sup> <sub>-0.07</sub>	keV
Line width $\sigma_{\text{Fe xxv}}$	0.01 <sup>+0.12</sup> <sub>-peg</sub>	0.04 <sup>+0.22</sup> <sub>-peg</sub>	keV
Line centre energy Fe $K\beta$	7.02 <sup>+0.07</sup> <sub>-0.04</sub>	7.00 <sup>+0.05</sup> <sub>-0.21</sub>	keV
Line width $\sigma_{\text{Fe } K\beta}$	0.09 <sup>+0.18</sup> <sub>-0.08</sub>	0.04 <sup>+peg</sup> <sub>-peg</sub>	keV
Reduced $\chi^2$ /d.o.f	179.5/175	164.1/196	

NOTE: *f* – marks a fixed parameters, *peg* – indicates a zero error, *d.o.f* – degrees of freedom.

CIAO software package. The data were grouped by `group_snr()` to set the minimum value signal-to-noise ratio for each bins and fitted using Sherpa (Freeman et al. 2001) fitting application.

The spectra were described in energy range 5.5–7 keV using simple phenomenological model that includes the power law (`xszpowerlw`), Galactic absorption (`xsphabs`), and absorption on the line-of-sight (`xszphabs`). We also added the Gaussian profiles (`xszgauss`) for model of the neutral Fe  $K\alpha$  fluorescent emission line at 6.4 keV, He-like iron Fe xxv  $K\alpha$  emission line at 6.7 keV and Fe  $K\beta$  fluorescent emission line at 7.08 keV. The photon indices were fixed for nuclei with value  $\Gamma = 1.75$ . Detailed broadband analysis for continuum spectrum is presented in Puccetti et al. (2016) and Nardini (2017). Finally the model in Sherpa was described as follows:

$$\text{xsphabs} * (\text{xszpowerlw} * \text{xszphabs} + \text{xszgauss} + \text{xszgauss} + \text{xszgauss})$$

We compiled the best-fitting parameters in Table 1. The Fe  $K\alpha$  best-fit values are  $E_{\text{N}} = 6.41^{+0.01}_{-0.02}$  keV and  $E_{\text{S}} = 6.39^{+0.01}_{-0.02}$  keV for N and S nuclei respectively. Therefore, line shift  $\Delta E \approx 0.02$  keV can be interpreted as the result of the motion of each nucleus around the centre of mass. The Fe  $K\alpha$  emission lines widths are  $\sigma_{\text{N}} = 0.05^{+0.01}_{-0.02}$  keV and  $\sigma_{\text{S}} = 0.05^{+0.04}_{-0.03}$  keV for N and S nuclei respectively. Such values

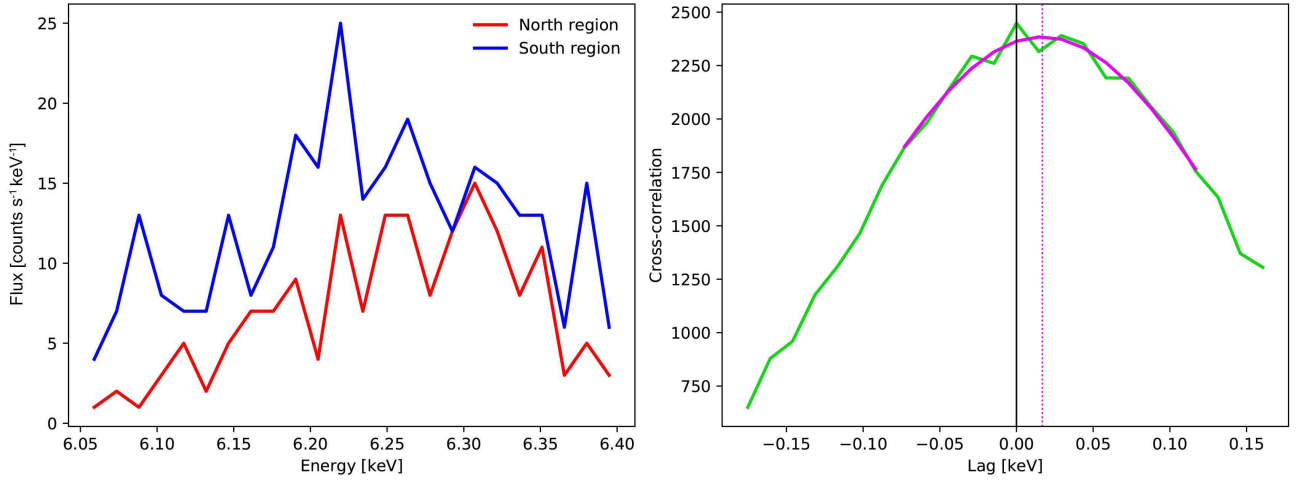


**Figure 2.** The original X-ray spectra for N and S nuclei (left) and their cross-correlation (right – green line). The magenta curve on the right panel corresponds to a best-fitting Gaussian, where the position of its centre is shown by the magenta dashed line.

of emission lines widths mean that the Fe  $K\alpha$  line is a narrow one. The emission lines at  $6.72^{+0.06}_{-0.05}$  and  $6.66^{+0.06}_{-0.07}$  keV can be explained as a highly ionised Fe xxv emission from circumnuclear starburst regions (Wang et al. 2014b).

## 2.2 Mass estimation

Assuming that N and S nuclei have formed the bound system and move around the mass centre we can estimate the enclosed mass. Based on the energy shift  $\Delta E$  of the observed Fe  $K\alpha$  lines and their line centre mean energy  $E_{\text{obs}} = 0.5(E_N + E_S)$  from Table 1 we obtained the velocity shift:

$$\Delta v_{\text{obs}} = \frac{\Delta E c}{E_{\text{obs}}} \approx 937 \text{ km s}^{-1}, \quad (2)$$

where  $\Delta E$  is the energy shift between two nuclei. We collected velocity differences from other bands in Table 2 and found that in comparison with optical/IR and radio observations our  $\Delta v_{\text{obs}}$  is a factor of three higher. Should be mentioned that this comparison is restricted by several limitations: (i) in most cases values were obtained after simple visual inspection of velocity maps, which also limited us in velocity error estimations; (ii) different AGNs' coordinates were used in observations, which complicated maps matching in different bands; (iii) the chosen of the region for velocity extraction is unclear, also are complicated by resolutions in different bands (from  $0''.5$  in X-ray band to  $0''.03$  in mm band). We assume that this discrepancy can be explained with the model where the X-ray and optic/radio bands emission is created in physically different regions at significantly different distances from the central BH.

In interacting galaxy NGC 6240 we expected that the emission in Fe  $K\alpha$  line created in a pc scale (inside the gas-dusty torus; see e.g. Nandra 2006) in contrast with the observed optic/IR emission which comes from the distance of tens of pc from the central SMBH. Recent studies of bright nearby AGN ( $z < 0.5$ ) with *Chandra* and *XMM-Newton* data are showed that with high probability for 24 objects the narrow Fe  $K\alpha$  line is emitting from the inner 1 pc around SMBH (Andonie et al. 2022). The next generation of planned space-born X-ray observatories includes *Athena* proposed by ESA (Nandra et al. 2013; Barret et al. 2018) and *Lynx* proposed by NASA (The Lynx Team 2018; Gaskin et al. 2019). They are ex-

**Table 2.** Absolute velocity difference between nuclear regions from X-ray, radio and optic/IR bands.

Band	Instrument	Line	$\Delta v$	Resolution	Reference <sup>†</sup>	
			km s <sup>-1</sup>	"	pc	
X-ray	<i>Chandra</i>	Fe $K\alpha$	937	0.5	245	This paper
NIR	SINFONI	CO(2-0)+CO(3-1)	$252 \pm 15$	0.1	49	[1]
NIR	SINFONI	H <sub>2</sub>	250	0.5	245	[2]
NIR	SINFONI	[O III] $\lambda 5007$	150	0.5	245	[2]
IR	MUSE	Ca II $\lambda\lambda 8498, 8542, 8662$	$144 \pm 42$	0.03	15	[3]
IR	MUSE	[N II] $\lambda 6548$	$160 \pm 54$	0.03	15	[3]
IR	MUSE	[O I] $\lambda 6300$	$262 \pm 24$	0.03	15	[3]
Radio	ALMA	CO(3-2)	250	0.3	147	[4]
Radio	ALMA	CO(6-5)	100	0.3	147	[4]
Radio	ALMA	<sup>12</sup> CO(2-1)	300	0.03	15	[5]
Radio	IRAM	H <sub>2</sub>	200	0.1	49	[1]

<sup>†</sup>References: [1] Engel et al. (2010), [2] Müller-Sánchez et al. (2018), [3] Kollatschny et al. (2020), [4] Fyhrie et al. (2021) [5] Treister et al. (2020).

pected to have a higher  $\sim 100$  times spectral resolution on 6 KeV, which can make clear the nature of the observed Fe  $K\alpha$  line.

The dynamical mass can be written in terms of observed velocity shift:

$$M_{\text{dyn}} \approx \frac{\Delta R \Delta v_{\text{obs}}^2}{G}, \quad (3)$$

where  $\Delta R$  is the separation and  $G$  is the gravitational constant. Using maximum projected distance  $\Delta R_{\text{proj}} = 1$  kpc as a estimation for the minimum physical separation of SMBHB  $\Delta R = \Delta R_{\text{proj}}$  we obtained the total dynamical mass within this region  $M_{\text{dyn}} \approx 2.04 \times 10^{11} M_{\odot}$ . Of course, our dynamical mass estimation affected by the underlying assumptions about the simple geometry of the NGC 6240 central region. As a first approximation, we assume that the projected separation of the nuclei is a intrinsic size of the system. We also assume that the observed velocity shift between nuclei is a real velocity difference. The current simple assumptions we use as a basis for our BHs dynamical merging time estimation at a first order. The detail parameter study of the possible different orientation and projection of the nuclei we keep beyond the scope of the current paper.

According to the empirical correlation between SMBH and galaxy

bulge masses (Kormendy & Ho 2013), and due to active merging galaxy state we estimated the maximum SMBHB total mass  $M_{\text{BH}12} = 0.01M_{\text{dyn}} \approx 2.04 \times 10^9 M_{\odot}$ . The obtained mean mass  $M_{\text{BH}}$  is comparable with the dynamical masses previously derived by Medling et al. (2011) and Kollatschny et al. (2020).

The difference  $\Delta E$  between the Fe  $K_{\alpha}$  lines centroids in spectra of both nuclei is the same order as the errors of two line's positions. Therefore, we performed additional validation of the estimated difference  $\Delta E$ , using the cross-correlation between N and S nuclei spectra (Fig. 2, left). The cross-correlation between original spectra is presented in Fig. 2 (right), where the magenta line is the fitted Gaussian function. The best-fitting position of the Gaussian profile is  $0.0170 \pm 0.0019$  keV, which is consistent with the estimated shift that we got from spectral fitting within the errors.

### 3 NUMERICAL MODELLING SMBH PARTICLES

For our simulations we used our own developed and publicly available  $\varphi$ -GPU<sup>3</sup> code with the blocked hierarchical individual time step scheme and a 4<sup>th</sup>-order Hermite integration scheme of the equation of motions for all particles (Berczik et al. 2011; Berentzen et al. 2008). The current version  $\varphi$ -GPU code uses a native GPU support and direct code access to the GPU using the NVIDIA CUDA library. The multi GPU support is achieved through the global MPI parallelisation. Each MPI process uses only a single GPU, but usually up to four MPI processes per node are started (in order to effectively use the multi core CPUs and the multiple GPUs on our clusters). More details about the  $\varphi$ -GPU code public version and its performance we are presented in Khan et al. (2018a) and Fiestas et al. (2012). The present code is well tested and already used to obtain important results in our earlier large scale (up to few million body) simulations (Zhong et al. 2014; Khan et al. 2018b; Li et al. 2012; Wang et al. 2014a). For simulations with lowest particle number  $N = 100\text{k}$  we used the GLOWOOD GPU cluster at MAO NASU. The main part of our numerical experiments with the largest particle number ( $N = 500\text{k}$  and  $200\text{k}$ ) we run on the JUWELS GPU cluster of the Jülich Supercomputing Centre.

In the current implementation of the code, we used a post-Newtonian ( $\mathcal{PN}$ ) formalism for the SMBHB relativistic orbit calculation. In this case, the equation of motion is usually presented as a power series  $1/c$  of light velocity, where  $n$ - $\mathcal{PN}$  is proportional to  $(v/c)^{2n}$ . The acceleration of the  $i$  binary particle from  $j$  particle with mass  $m_j$  one can write in the following form:

$$\mathbf{a}_i = -\frac{Gm_j}{R^2} [(1 + \mathcal{A}n_{ij}) + \mathcal{B}\mathbf{v}_{ij}], \quad (4)$$

where  $R$  is the separation between  $i$  and  $j$  binary particles,  $\mathbf{n}_{ij}$  is the normalised position vector and  $\mathbf{v}_{ij}$  is the relative velocity vector. The classic Newtonian acceleration has explicit representation in equation (4), when  $\mathcal{PN}$  corrections are contained in two coefficients  $\mathcal{A}$  and  $\mathcal{B}$ :

$$\mathcal{A} = \frac{\mathcal{A}_{1\mathcal{PN}}}{c^2} + \frac{\mathcal{A}_{2\mathcal{PN}}}{c^4} + \frac{\mathcal{A}_{2.5\mathcal{PN}}}{c^5} + O\left(\frac{1}{c^6}\right), \quad (5)$$

$$\mathcal{B} = \frac{\mathcal{B}_{1\mathcal{PN}}}{c^2} + \frac{\mathcal{B}_{2\mathcal{PN}}}{c^4} + \frac{\mathcal{B}_{2.5\mathcal{PN}}}{c^5} + O\left(\frac{1}{c^6}\right), \quad (6)$$

where  $1\mathcal{PN}$  and  $2\mathcal{PN}$  are the non-dissipative terms that 'conserve' the energy of the system and are revealed in the precession of the

**Table 3.** List of parameters for physical model.

Nucleus	$\Delta R$	$M_*$	$Q$	$a$	$M_{\text{BH}}$	$q$
	kpc	$10^{10} M_{\odot}$		pc	$10^8 M_{\odot}$	
(1)	(2)	(3)	(4)	(5)	(6)	(7)
1 (N)	1	13.60	0.5	200	13.60	0.5
2 (S)	–	6.80	–	159	6.80	–

NOTE: (1) nuclei ID, (2) initial separation for central BHs, (3) total stellar mass, (4) stellar mass ratio  $Q = M_{*2}/M_{*1}$ , (5) Plummer radius, (6) masses of the BHs, (7) mass ratio for the BHs  $q = M_{\text{BH}2}/M_{\text{BH}1}$ .

orbital pericenter. The  $2.5\mathcal{PN}$  is the dissipative term that 'carries out' energy from the system due to GWs emission. Coefficients  $\mathcal{A}$  and  $\mathcal{B}$  are the functions of individual masses, individual velocities, separation and normalised vector. Their full expressions can be found in Blanchet (2006, equation 168). The detailed references and complete descriptions of the equation of motion in  $\mathcal{PN}$  formalism up to  $3.5\mathcal{PN}$  can be found at Blanchet (2006), Kupi et al. (2006), Berentzen et al. (2008), Berentzen et al. (2009), Brem et al. (2013), Sobolenko et al. (2017).

Detailed study of the turning on one-by-one  $\mathcal{PN}$  corrections show requirement to including all  $\mathcal{PN}$  terms up to highest wanted order (Berentzen et al. 2009). Adding conservative  $1\mathcal{PN}$  and  $2\mathcal{PN}$  corrections remarkably change orbits during three-body encounters and can reduce binary merging time two times. We applied all  $\mathcal{PN}$  corrections up to order  $O(1/c^6)$ , so the  $2.5\mathcal{PN}$  correction is the highest order that we took into account.

## 4 SYSTEM INITIAL CONFIGURATIONS

### 4.1 Physical model and units

The evolution of the central parts of the merging galaxies is closely related to the dynamical processes of the SMBHB evolution. The stars located in the merging galactic centre can interact directly with the SMBHB. Such stars in close orbits around the SMBHB can take away a significant part of the SMBHB angular momentum and energy after the typical three-body gravitational scattering. As a result the semimajor axis of the binary system monotonically decreases. This process we usually call SMBHB 'hardening' (Merritt & Ferrarese 2001; Merritt 2001). Very precise individual orbit calculation of the merging SMBHB in a dense stellar environment gives the correct description of binary system parameters evolution.

We started the galaxy merger from the dynamical system of two unbound central SMBHs with the separation  $\Delta R = 1$  kpc according to our estimations in Section 2.2 (Table 3). Each SMBH is surrounded by its own bound stellar systems with simple Plummer density distribution (Plummer 1911):

$$\rho(r) = \frac{3M_0}{4\pi a^3} \left(1 + \frac{r^2}{a^2}\right)^{-\frac{5}{2}}, \quad (7)$$

which produce the cumulative mass distribution:

$$M(< r) = M_0 \frac{r^3}{(r^2 + a^2)^{3/2}}, \quad (8)$$

where  $M_0$  is the total mass of each galactic bulge, and  $a$  is a scale factor that characterises the size of each nucleus (Plummer radius). Due to the flat central distribution of the Plummer profile, the SMBHB hardening as the assuming numerical hardening will be smaller compared to the more peaked core distribution profiles (Jaffe

<sup>3</sup> <https://github.com/berczik/phi-GPU-mole>

**Table 4.** List of parameters for basic and mass prescription numerical models.

$N$	RAND	$m_{\text{HMP}}:m_{\text{LMP}}$	$m_{\text{HMP}}$ $10^6 M_{\odot}$	$m_{\text{LMP}}$ $10^6 M_{\odot}$	$\mathcal{PN}$
(1)	(2)	(3)	(4)	(5)	(6)
100k	1, 2, 3	10:1	10.20	1.130	1
200k	1, 2, 3	10:1	5.10	0.567	2
500k	1, 2, 3	10:1	2.04	0.227	3
100k	1	1:1	–	2.400	–
100k	1	5:1	5.10	1.280	–
100k	1	20:1	20.40	1.070	–

NOTE: (1) total number of particles, (2) randomisation seed number, (3) HMPs to LMPs mass ratio, (4) and (5) mass of HMPs and LMPs respectively, (6) randomisation seed number for which we turned  $\mathcal{PN}$  correction.

1983; Hernquist 1990; Dehnen 1993). Using Plummer distribution we model the minimum numerical hardening for our SMBHB.

Previously estimated from observations dynamical mass is assumed as the total mass of the stellar component  $M_{*,\text{tot}} = M_{\text{dyn}} = 2.04 \times 10^{11} M_{\odot}$ . Corresponding to Section 2.2 the mass of the SMBHB is set  $M_{\text{BH}12} = 2.04 \times 10^9 M_{\odot}$ . Supposing the major merging we used for the mass ratio of the galactic bulges and the central BH's 2:1 ratio. According to this assumption the primary (heavier) bulge with mass  $M_{*,1} = 1.36 \times 10^{11} M_{\odot}$  contains BH with mass  $M_{\text{BH}1} = 1.36 \times 10^9 M_{\odot}$  and secondary (lighter) bulge with mass  $M_{*,2} = 6.8 \times 10^{10} M_{\odot}$  contains BH with mass  $M_{\text{BH}2} = 6.8 \times 10^8 M_{\odot}$  (Table 3). Also for further reference we calculated the Schwarzschild radius of the SMBHB as  $R_{\text{SW}12} = 2GM_{\text{BH}12}/c^2 = 195 \mu\text{pc}$ .

For the first bulge we assumed the Plummer radius near equal to the influence radius of the BH, that give  $a_1 = 0.2\Delta R = 200 \text{ pc}$ . For the second (smaller) bulge we set the Plummer radius proportionally smaller, assuming the same central density in both bulges, that is  $a_2 = 0.5^{1/3}a_1 \approx 159 \text{ pc}$  (Table 3). The initial orbital velocities of the merging galactic bulges (together with the BH's) we set as that the orbital eccentricity (in point mass approximation) equals to  $ecc_0 = 0.5$ .

For the numerical scaling we used the N-body normalisation (Hénon 1971)<sup>4</sup>. The physical units was choosing according to estimations for total stellar mass and maximum projected separation between BHs:

$$M_{\text{NB}} = M_{\text{dyn}} = 2.04 \times 10^{11} M_{\odot}, \quad (9)$$

$$R_{\text{NB}} = \Delta R = 1 \text{ kpc}. \quad (10)$$

In N-body system of units we have for velocity and time units the rescaling values:

$$V_{\text{NB}} = 936.7 \text{ km s}^{-1}, \quad (11)$$

$$T_{\text{NB}} = 1.04 \text{ Myr}. \quad (12)$$

In this system of units (Sobolenko et al. 2017) for the light speed we got the value:  $c = 320 V_{\text{NB}}$ .

## 4.2 Numerical models

To check the numerical convergence of our Newtonian dynamical ‘hardening’ timescale results we used three different total particle numbers for the system  $N = 100\text{k}$ ,  $200\text{k}$ , and  $500\text{k}$ . For each of these particle numbers, we run a separate set of simulations with three

**Table 5.** Timescales for models with turned on  $\mathcal{PN}$  terms.

$N$	RAND	$t_b$ Myr	$t_{\mathcal{PN}\text{beg}}$ Myr	$t_{\text{merge}}$ Myr
(1)	(2)	(3)	(4)	(5)
100k	1	3.77	10.4	43.6
200k	2	3.90	10.4	34.7
500k	3	3.77	10.4	30.5
500k	A.18 <sup>a</sup>	5.15	23.5	40.3
500k	A.25 <sup>a</sup>	5.15	32.7	46.7

NOTE: (1) total number of particles, (2) randomisation seed number for which we turned  $\mathcal{PN}$  correction, (3) binding binary time, (4) time for turning  $\mathcal{PN}$  correction, (5) merging time. <sup>a</sup>Model A from S21.

different particle random seeds  $\text{RAND} = 1, 2, 3$  (Table 4, top three numerical models). Below we will use the abbreviation 100-1 for a run with particle number  $N = 100\text{k}$  and random seed  $\text{RAND} = 1$ . In all of these nine basic runs, we generated two different types of particles for each galaxy (completely mixed inside the system), the so-called ‘high mass’ (HMPs) and ‘low mass’ particles (LMPs). We fixed the individual particles’ mass ratio for these particles as 10:1. For all the nine runs we also used the fixed number ratio for the HMPs and LMPs particle number:  $N_{\text{HMP}}:N_{\text{LMP}} = 1:10$ . This small fraction of HMPs allowed us to mimic the dynamical influence of the giant molecular clouds and/or the compact stellar systems (globular clusters) on the common stellar system of the merging centres (colliding bulges). Even these small fraction of ‘super’ particles with a larger gravitational softening can have a great influence on the phase space mixing of the ‘normal’ stellar particles.

We also run three additional runs with  $N = 100\text{k}$  simulations using the different HMPs to LMPs individual mass ratio. In comparison to the basic runs, where we set the ratio 10:1, we run simulations with mass ratios 5:1, 20:1 and with just LMPs without HMPs 1:1 (Table 4, bottom three models). We specially carried out these three runs to illustrate the dynamical effect of the possible higher mass ratio of the particles.

For different number of particles we also set a different individual gravitational softening length. For the BH-BH particles interaction we used the exactly zero softening ( $\epsilon_{\text{BH}} = 0.0$ ). For the HMPs we used  $\epsilon_{\text{HMP}} = 10^{-4} R_{\text{NB}} = 0.1 \text{ pc}$  gravitational softening. For the LMPs we set  $\epsilon_{\text{LMP}} = 10^{-5} R_{\text{NB}} = 0.01 \text{ pc}$ . For the mixed interactions between the different type of particles we used the mixed gravitational softening between the particles:

$$\epsilon_{ij}^2 = 0.5(\epsilon_i^2 + \epsilon_j^2). \quad (13)$$

In a case, if one of the particles is a BH (or  $i$  or  $j$ ) we set the additional coefficient  $10^{-2}$  in front of the equation (13) to make a further extra reduction for such a gravitational interaction. As the result, we obtained effective softening parameters in level  $10^{-5} R_{\text{NB}} = 0.01 \text{ pc}$  and  $10^{-6} R_{\text{NB}} = 0.001 \text{ pc}$  for HMPs and LMPs respectively.

Leaned on the 9 basic Newtonian runs we run three full  $\mathcal{PN}$  runs to leading SMBHB to merging, where we turned on the extra  $\mathcal{PN}$  terms for the BH-BH gravitational interaction. Specially chosen three different Newtonian runs have different particle numbers and are noted with suffix  $\mathcal{PN}$  (Table 4, top three numerical models). The  $\mathcal{PN}$  terms turned on time  $t_{\mathcal{PN}\text{beg}} \approx 10 \text{ Myr}$  after the binary binding at time  $t_b$  (Table 5). We stopped these runs when the SMBH particles separation fell below  $\approx 4 R_{\text{SW}12}$  and this time assumed as merging time  $t_{\text{merge}}$  (Table 5). We also will compare our results with previous simulations, which consist of 4 physical and 16 numerical models (Sobolenko et al. 2021, hereafter S21).

<sup>4</sup> [https://en.wikipedia.org/wiki/N-body\\_units](https://en.wikipedia.org/wiki/N-body_units)

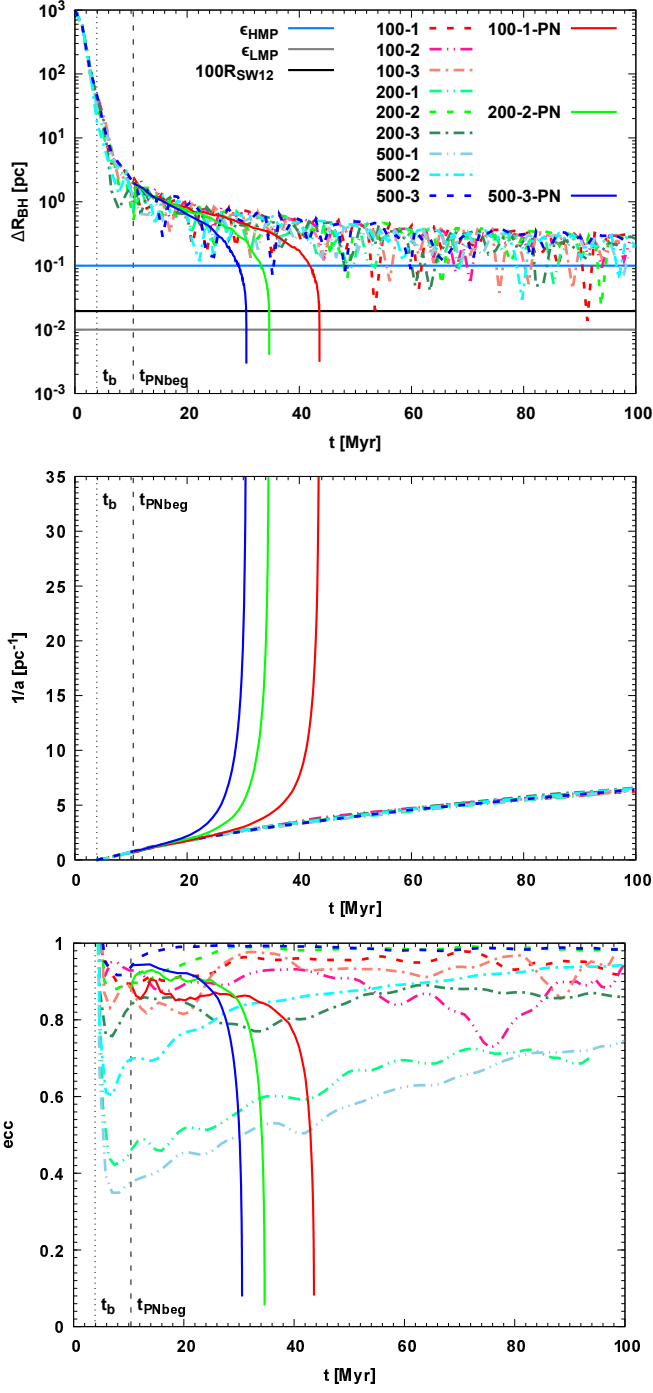


**Figure 3.** Evolution of SMBHB separation (top), inverse semimajor axis (middle) and eccentricity (bottom) for basic Newtonian (colour dashed lines) and  $\mathcal{PN}$  runs (colour solid lines) with mass ratios HMPs to LMPs 10:1 from Table 4. The red, green and blue solid lines are  $\mathcal{PN}$  runs for particle number 100k, 200k, and 500k, respectively. On the top panel, the horizontal solid light blue and grey lines are softening parameters for HMPs and LMPs respectively, the solid black line is 100 Schwarzschild radii. Vertical black dashed lines are binding time  $t_b$  for models 100-1, 200-2, 500-3 (Table 5) with following turning on  $\mathcal{PN}$  terms at time  $t_{\mathcal{PNbeg}}$  (Table 5).

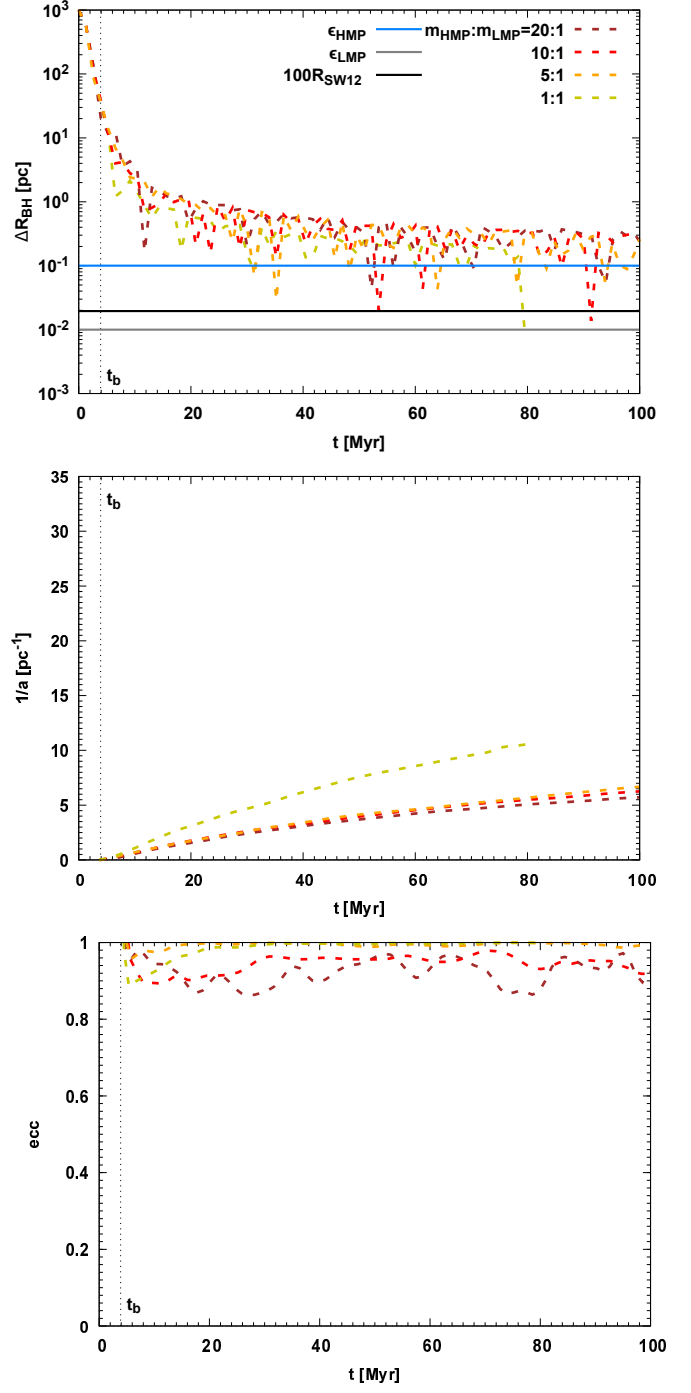


**Figure 4.** Evolution of SMBHB separation (top), inverse semimajor axis (middle) and eccentricity (bottom) for Newtonian runs (dashed lines) with number of particles  $N = 100\text{k}$ , randomisation seed  $\text{RAND} = 1$  and different mass ratios HMPs to LMPs  $m_{\text{HMP}}:m_{\text{LMP}} = 20:1, 10:1, 5:1, 1:1$  from Table 4. On the top panel, the solid light blue and grey lines are softening parameters for HMPs and LMPs, the solid black line is 100 Schwarzschild radii. The vertical black dashed line is binding time  $t_b$  for models (Table 5).

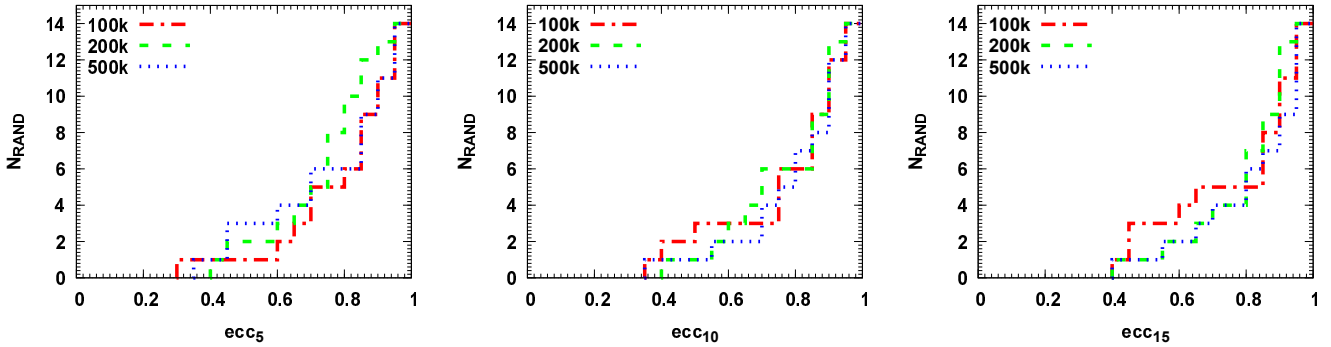


**Figure 5.** Eccentricity cumulative distributions for numerical models with different randomisation seeds (RAND) at different times from left to right:  $t = 5.2$  Myr (5 NB; bounding time), 10.4 Myr (10 NB; turning  $\mathcal{PN}$  terms) and 15.6 Myr (15 NB; forming hard binary). Colour show models with the different number of particles  $N$ : red – 100k, green – 200k, blue – 500k.

## 5 SIMULATION RESULTS AND DISCUSSION

### 5.1 Dynamical timescales

We describe the evolution of the SMBHB by the evolution of the binary orbit’s parameters, such as separation  $\Delta R$ , inverse semimajor axis  $1/a$  and eccentricity  $ecc$  (Fig. 3). As mentioned above, at time  $t = 0.0$  Myr the SMBH particles at initial separation  $\Delta R$  are not bound. In Newtonian N-body simulations the binary forms after several passages at binding time  $t_b$  in less than 4 Myr (Tables 5, 6). The evolution of separation (Fig. 3, top) and inverse semimajor axis (Fig. 3, middle) show a quite good agreement for a different number of particles and initial randomisation of N-body particles’ positions and velocities. This already made the results of our simulations quite independent from these purely numerical parameters. In comparison with model A (the closest model for our current research from S21) current basic numerical models shown an earlier ( $\approx 20\%$ ) binding time  $t_b$  (Table 5). In our set of runs, the bound binary is usually formed with a semimajor axis almost equal to the SMBHs influence radius.

For basic numerical models the eccentricity did not show any systematic dependence on the number of particles or randomisation seeds due to their very ‘stochastic’ nature. In the basic models with 100k particles, the binaries were formed with eccentricities from 0.84 to 0.94. For the basic 200k runs, we get the eccentricities in the range 0.42–0.88. For the basic 500k runs we get an even wider range 0.34–0.92 (similar to in S21). To make our conclusion more statistically significant we performed additional Newtonian N-body simulations for  $N = 100k, 200k, 500k$  with different randomisation seeds and as a result totally we have 14 runs for each  $N$ . SMBHs orbits show a smooth trend with the orbital eccentricity higher than 0.5 (Fig. 5). The orbital eccentricity slightly grows during the binary evolution (Preto et al. 2011). In Fig. 5 we present the cumulative eccentricity distribution for the three characteristic times (bounding time; time, when  $\mathcal{PN}$  terms turn on; a time when the hard binary forming). We do not have a substantial dependence on the particle numbers  $N$ . Our  $N$ -independent wide eccentricity range (0.40–0.99) for the binaries does not really support the predictions of a more narrow eccentricity spread as an increasing number of N-body particles (Rantala et al. 2017; Nasim et al. 2020).

After turning on the  $\mathcal{PN}$  terms at time  $t_{\mathcal{PN}beg} = 10 T_{NB} = 10.04$  Myr all our  $\mathcal{PN}$  runs show a quite short dynamical merging time  $t_{merge}$  comparable with obtained by Khan et al. (2016, 2018b) (Table 5). Basically all three different  $\mathcal{PN}$  models (100-1, 200-2,

500-3) merge in under  $\approx 44$  Myr (Table 5). Differences at the merging times can be explained by the strong effect of the eccentricities at the time when we turned on  $\mathcal{PN}$  corrections. Previous detailed study of 20 physical and numerical models showed that merging time for central SMBHB is less than 50 Myr (for full description see S21). But our current binary models can merge even earlier around 31 Myr (model 500-3), which can be explained by a higher eccentricity ( $\approx 0.9$ ) at the binary formation time than in S21.

To check the merging time dependency of our PN runs from the different randomisation seeds (RAND) for the particle distributions we carry out extra 10 runs of the 500-3-PN model (Table 6). Before starting the extra PN runs we estimated the bounding time  $t_b \approx 4$  Myr and hardening time  $t_h \approx 15$  Myr for each run. The SMBHB merging time varies in a range from 15.2 Myr to 56.8 Myr and, as we expect, mainly depends on the initial eccentricity after the moment of the binary formation (Fig. 6). From our limited sample (totally 11  $\mathcal{PN}$  simulations) we already can conclude that the merging time can be approximated as a quite shallow function of the eccentricity:

$$t_{merge} = A \times \left[ 1 - (ecc_{10})^2 \right]^B, \quad (14)$$

where coefficients  $A = 71.98 \pm 7.89$  and  $B = 0.46 \pm 0.07$ . As a basic conclusion from these extra 10 runs, we can state that even for the very small initial eccentricity the merging time has the upper limit around  $\approx 70$  Myr.

In the Fig. 4 we show the results from our extra runs with 100k particles (Table 4, tree bottom models), which we started to check the effect of different HMPs to LMPs mass ratios ( $m_{HMP}:m_{LMP} = 20:1, 10:1, 5:1, 1:1$ ). Our runs with mass prescriptions show a qualitatively similar evolution in separation, inverse semimajor axis and even eccentricity. For the inverse semimajor axis  $1/a$  (Fig. 4, middle) we see the trend, that is more significant at time  $\approx 100$  Myr. This trend strongly depends on the limit close to the 1:1 particles mass ratio and is determined by the mass of LMPs (see Table 4 for  $m_{LMP}$ ). Because we always have a larger amount of LMPs (i.e. more interaction with the LMP particles), the binary hardening always more strongly depends on the LMPs masses. The small amount of HMPs ( $\approx 9\%$ ), in each mass prescription model, apparently is not enough for extracting sufficient energy amount during three-body encounters with the binary SMBH. For a quantitative description of this process, a detailed study of energy balance is required (for example as it was made by Avramov et al. 2021).

For mass prescription models the eccentricity (Fig. 4, bottom) varies in a narrower range 0.85-0.99 than for basic numerical runs



**Table 6.** Timescales for additional numerical models with  $N = 500k$  and different randomisation seeds.

RAND	$t_b$	$t_h$	$t_{\text{merge}}$
(1)	Myr (2)	Myr (3)	Myr (4)
4	4.10	14.04	38.4
5	4.13	14.95	40.0
6	4.10	14.60	15.2
7	4.04	12.87	19.1
8	4.03	13.40	24.7
9	4.10	15.34	27.2
10	4.16	14.69	46.0
11	3.87	13.91	20.9
12	4.16	14.04	56.8
13	4.06	14.30	38.1

NOTE: (1) randomisation seed number for which we turned  $\mathcal{PN}$  corrections, (2) binding binary time, (3) form hard binary time, (4) merging time.

(Fig. 3, bottom). We do not see any strong dependence of the binary initial eccentricity from the LMPs particles individual masses. Lines for different models are very often overlapping (crossing). We can just note that models with higher mass ratios (20:1, 10:1) have some kind of ‘bumps’. This can indicate the interaction with the particular HMP. Even if their number are much lower compare to the LMP such a small amount of high mass field particles can play a significant role in the binary eccentricity behaviour.

## 5.2 Gravitational waves

For our model with maximum  $N$  and turning on  $\mathcal{PN}$  terms ( $N = 500k$ ,  $\text{RAND} = 3$ ,  $m_{\text{HMP}}:m_{\text{LMP}} = 10:1$ ) we also calculated the expected amplitude-frequency picture for SMBHB merging in NGC 6240. For the simple waveform calculation we used the GW quadrupole term expressions from Kidder (1995) (also see Brem et al. 2013; Sobolenko et al. 2017):

$$h^{ij} = \frac{2G\mu}{D_L c^4} \left[ Q^{ij} + P^{0.5} Q^{ij} + P Q^{ij} + P^{1.5} Q^{ij} + \dots \right], \quad (15)$$

where  $P$  is a correction term for corresponding  $\mathcal{PN}$  order,  $\mu$  is the reduced mass,  $D_L$  is the luminosity distance between the origin of the reference frame and the source, and  $Q^{ij}$  is the quadrupole term. The last one can be written in the form:

$$Q^{ij} = 2 \left[ v^i v^j - \frac{GM_{\text{BH}12}}{r} n^i n^j \right], \quad (16)$$

where  $v^i$  and  $n^i$  are the relative velocity and normalised position vectors in this reference frame respectively.

For illustrative purpose we did not highly accurate model waveforms and neglected the higher order terms. In this assumption we calculated the tensor in the source frame simply by:

$$h^{ij} \approx \frac{4G\mu}{D_L c^4} \left[ v^i v^j - \frac{GM_{\text{BH}12}}{r} n^i n^j \right]. \quad (17)$$

For the sake of simplicity, we choose the virtual detector to be oriented such that the coordinate axes coincide with the source frame. It allowed us did not make any coordinate transformations. We computed  $h_+$  and  $h_\times$  from  $h^{ij}$ , which gave the relevant measurable strains in ‘+’ and ‘ $\times$ ’ polarisations (Brem et al. 2013; Sobolenko et al. 2017).

The standard resolution for our  $\mathcal{PN}$  runs was  $1.3 \times 10^5$  years. We extracted the SMBH particles data (positions & velocities) from the last available  $\mathcal{PN}$  model’s snapshot to calculate the final stage of

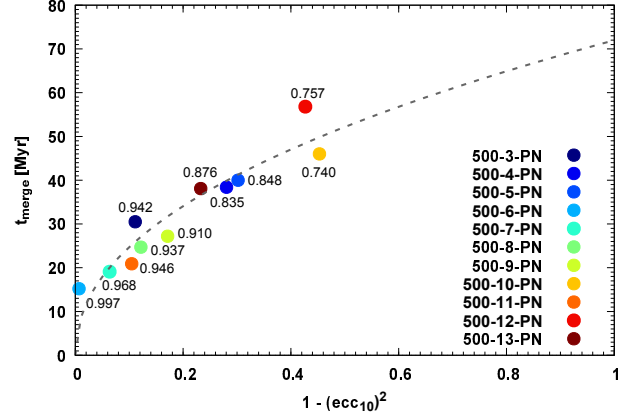


**Figure 6.** SMBHB merging time as function of eccentricity at time  $t = 10.4$  Myr (10.0 NB), when we started  $\mathcal{PN}$  runs. Colour show models with different randomisation seeds RAND and numbers show the eccentricity values. Grey dashed line is fitting function (see equation 14).

the SMBH merger (up to  $\approx 4R_{\text{SW}12}$ ) with the high resolution. Using these particle data, we followed only the two SMBHs dynamical  $\mathcal{PN}$  evolution. For this purpose, we used our highly accurate two-body Hermite integrator. We run these separate simulations with the maximum possible accuracy, keeping at minimum 100 points per SMBH particles orbital integration, which give us time resolution up to  $\sim 3$  days.

The calculated waveforms for  $h_+$  polarisation and amplitude-frequency picture from the final phase of our model runs (last 50 years and zoomed last 10 years evolution before the merger) we present in Fig. 7. It is worth noting that  $\mathcal{PN}$  approximation works well for describing the early inspiral SMBHBs, and numerical relativity and perturbation theory should be used for full waveforms picture of merging event and ringdown (for reference see Le Tiec 2014). Obtained frequencies for merging events from such high mass SMBHBs ( $\sim 10^{8-9} M_\odot$ ) at such distances ( $D_L = 111.2$  Mpc) lay on sensitive curve of current and future pulsar timing array (PTA) consortium’s: European PTA (EPTA, Kramer & Champion 2013), Parkes PTA (PPTA, Hobbs 2013), North American Nanohertz Observatory for Gravitational Waves (NANOGrav, Ransom et al. 2019), which collectively form International PTA (IPTA, Manchester & IPTA 2013). Such detection of individual SMBHBs merging and GWs stochastic background (see the recent NANOGrav 12.5 yr data set results at Arzoumanian et al. 2020) will be strong evidence of the possibility of SMBHBs binding, their reaching sub-pc scale, merging and emitting GWs.

## 6 CONCLUSIONS

In this paper, we investigated the X-ray properties of dual AGN in NGC 6240 using *Chandra* observations in the 0.5–7.5 keV and performed numerical N-body simulations based on the results of the corresponding spectral analysis. The main conclusions of this study can be summarised as follows.

- (i) We performed X-ray analysis of the combined spectrum from four *Chandra* observations of NGC 6240 with resulting exposure of 480 ks for each of two active nuclei. These spectra demonstrated individual Fe  $K\alpha$  emission lines with observational energies  $E_S = 6.39^{+0.01}_{-0.02}$  keV and  $E_N = 6.41^{+0.01}_{-0.02}$  keV with corresponding line

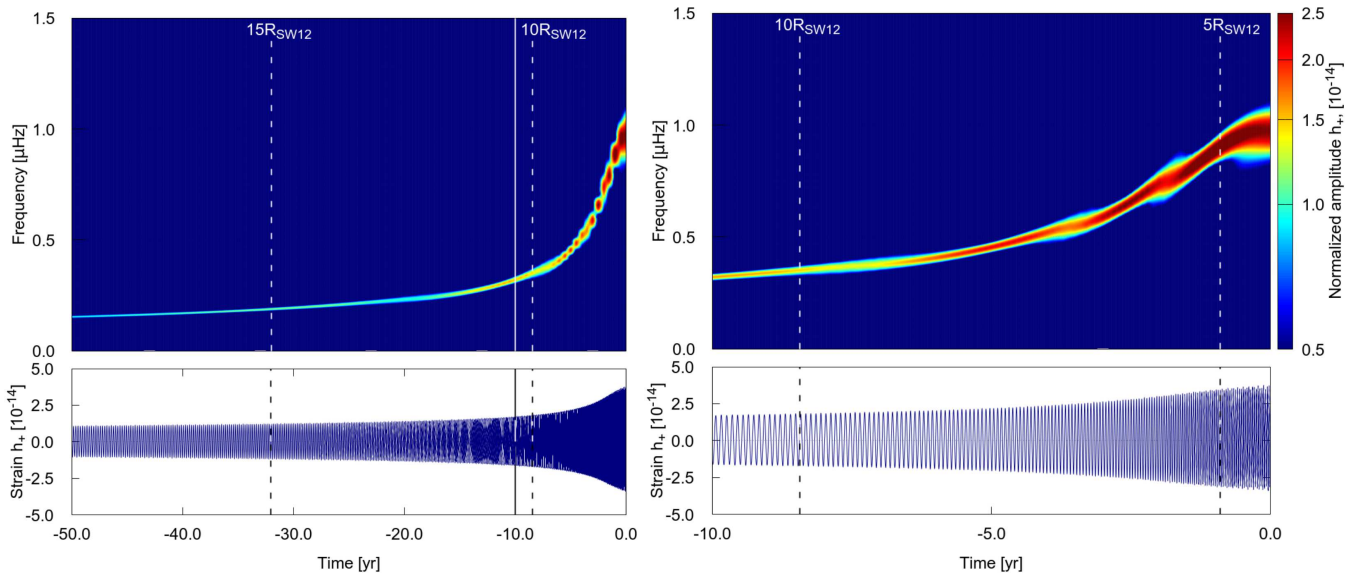


**Figure 7.** Time-frequency representations (top) of the strain data (bottom) for predicted gravitational waveforms of  $h_+$  polarisation from SMBHB merging at NGC 6240 ( $D_L = 111.2$  Mpc) for the last 50 yr (left) and last 10 yr (right). Major merging is represented by binary component with masses  $1.36 \times 10^9 M_\odot$  and  $6.8 \times 10^8 M_\odot$  and corresponding mass ratio 2:1. The final separation (due to our  $\mathcal{PN}$  routine) is 0.75 mpc. The solid vertical line on the left panel indicates the last 10 yr of merging. Dashed vertical lines from left to right indicate binary separation 15, 10 and 5 Schwarzschild radii respectively.

widths  $\sigma_S = 0.05^{+0.04}_{-0.03}$  keV and  $\sigma_N = 0.05^{+0.01}_{-0.02}$  keV for South and North nuclei respectively.

(ii) We estimated the dynamical mass for these nuclei as  $M_{\text{dyn}} \approx 2.04 \times 10^{11} M_\odot$  from X-ray analysis assuming that obtained energy shift caused by the relative motion of the two nuclei at the late stage. Accepting that this mass represents the mass of bulge, we estimated SMBHB mass as  $M_{\text{BH}12} \approx 2.04 \times 10^9 M_\odot$ . This value is comparable with estimations by other authors (Medling et al. 2011; Kollatschny et al. 2020).

(iii) Based on the estimated bulge mass and maximum projected separation  $\Delta R = 1$  kpc of the central SMBHB we constructed a physical model of the merging system. Using this physical model we made twelve basic numerical models' realisations with different particles number  $N = 100\text{k}, 200\text{k}, 500\text{k}$ . To obtain the merging time we run Newtonian and  $\mathcal{PN}$  N-body models (up to  $2.5\mathcal{PN}$  term). As a basic code, we used our own direct N-body  $\varphi$ -GPU code with 4<sup>th</sup> order Hermite integration scheme and individual timesteps for particles.

(iv) All basic Newtonian simulations showed a very good alignment in inverse semimajor axis evolution. From these runs, we concluded the independence of our SMBH binary hardening results on the initial number of particles (100k, 200k, and 500k) and randomisation for particles' positions and velocities. The eccentricity did not show any systematic dependence neither on the number of particles nor randomisation seeds due to its very 'stochastic' nature.

(v) To make our conclusions more statistically significant we performed extra Newtonian N-body simulations for  $N = 100\text{k}, 200\text{k}, 500\text{k}$  with different randomisation seeds. For extra simulations, eccentricity also did not show any substantial dependence on the particle numbers  $N$ . Our  $N$ -independent wide eccentricity range (0.40–0.99) for the binaries does not support the predictions (Rantala et al. 2017; Nasim et al. 2020) of a more narrow eccentricity spread as an increasing number of N-body particles.

(vi) To estimate the merging time for a central SMBHB we combined the basic Newtonian and  $\mathcal{PN}$  numerical models. The obtained merging times lay in a range from 15 Myr to 57 Myr, which is

in quite good agreement with our previous results (Sobolenko et al. 2016, 2021). The extra ten  $\mathcal{PN}$  Newtonian and  $\mathcal{PN}$  models with  $N = 500\text{k}$  and different randomisation seeds for the particle distributions show also a quite similar result. Based on the numerical approximation of the merging time as a function of SMBH binary eccentricity we can conclude that even for the possibly very small initial eccentricity the merging time anyway has an upper limit around  $\approx 70$  Myr.

(vii) Implementing relativistic  $\mathcal{PN}$  approximation up to  $2.5\mathcal{PN}$  terms allowed us to follow the SMBHB evolution till the mpc scale. We obtained the waveforms and amplitude-frequency maps for the last 50 and 10 years for the SMBHB system in interacting galaxy NGC 6240. Such SMBHBs merging events can be observed in the current and future PTA campaigns.

The presented complete research from observation analysis to numerical modelling gives us a powerful key for detailed investigation of the complex objects such as double/multiple AGN systems at different merging stages.

## ACKNOWLEDGEMENTS

The authors thank for the anonymous referee for the fruitful comments and corrections of our mistakes/typos in the manuscript. We believe, that her/his useful comments greatly improved the final version of our paper.

The authors gratefully acknowledge the Gauss Centre for Supercomputing (GSC) e.V. ([www.gauss-centre.eu](http://www.gauss-centre.eu)) for funding this project by providing computing time through the John von Neumann Institute for Computing (NIC) on the GCS Supercomputers JURECA and JUWELS at Jülich Supercomputing Centre (JSC). This research has made use of data obtained from the Chandra Data Archive and the Chandra Source Catalog, and software provided by the Chandra X-ray Center (CXC) in the application packages CIAO and Sherpa.

OK is grateful to Dr. O. Torbaniuk for useful discussions and comments and Dr. I. Vavilova for helpful remarks. OK acknowledge sup-

port by the budgetary program ‘Support for the development of priority fields of scientific research’ (CPCEL 6541230), project No. 10-F, and the Target Complex Program of Scientific Space Research of the NAS of Ukraine. OK thanks the Astronomical Observatory of the Jagiellonian University for support during the International Summer Student Internship, where a part of this work was done.

The work of VM was supported by the Polish NSC grant 2016/22/E/ST9/00061.

MS acknowledges the support under the Fellowship of the National Academy of Sciences of Ukraine for young scientists 2020-2022. PB and MS acknowledge support by the Volkswagen Foundation in Germany under the grant No. 97778. The work of PB was also supported by the Volkswagen Foundation under the special stipend No. 9B870 (2022).

PB and BS also acknowledges the support from the Science Committee of the Ministry of Education and Science of the Republic of Kazakhstan (Grant No. AP08856149). PB thanks the support by Ministry of Education and Science of Ukraine under the France - Ukraine collaborative grant M2-16.05.2022. PB express acknowledge the support by the National Academy of Sciences of Ukraine under the Main Astronomical Observatory GPU computing cluster project No. 13.2021.MM.

The work of PB, AV and MS was supported under the special program of the NRF of Ukraine ‘Leading and Young Scientists Research Support’ – ‘Astrophysical Relativistic Galactic Objects (ARGO): life cycle of active nucleus’, No. 2020.02/0346.

BS acknowledges the Nazarbayev University Faculty Development Competitive Research Grant Program No 11022021FD2912 (ssh2022007).

## DATA AVAILABILITY

The data underlying this article will be shared on reasonable request to the corresponding author.

## REFERENCES

Andonie C., et al., 2022, arXiv e-prints, p. [arXiv:2204.09469](https://arxiv.org/abs/2204.09469)  
 Arzoumanian Z., et al., 2020, *ApJ*, **905**, L34  
 Avramov B., Berczik P., Meiron Y., Acharya A., Just A., 2021, *A&A*, **649**, A41  
 Barausse E., 2012, *MNRAS*, **423**, 2533  
 Barger A. J., Cowie L. L., Sanders D. B., Fulton E., Taniguchi Y., Sato Y., Kawara K., Okuda H., 1998, *Nature*, **394**, 248  
 Barret D., et al., 2018, in den Herder J.-W. A., Nikzad S., Nakazawa K., eds, Society of Photo-Optical Instrumentation Engineers (SPIE) Conference Series Vol. 10699, Space Telescopes and Instrumentation 2018: Ultraviolet to Gamma Ray. p. 106991G ([arXiv:1807.06092](https://arxiv.org/abs/1807.06092)), doi:10.1117/12.2312409  
 Begelman M. C., Blandford R. D., Rees M. J., 1980, *Nature*, **287**, 307  
 Bennett C. L., et al., 2003, *ApJS*, **148**, 1  
 Berczik P., Merritt D., Spurzem R., Bischof H.-P., 2006, *Astrophys. J., Lett.*, **642**, L21  
 Berczik P., et al., 2011, in International conference on High Performance Computing, Kyiv, Ukraine, October 8-10, 2011. pp 8–18  
 Berentzen I., Preto M., Berczik P., Merritt D., Spurzem R., 2008, *Astronomische Nachrichten*, **329**, 904  
 Berentzen I., Preto M., Berczik P., Merritt D., Spurzem R., 2009, *ApJ*, **695**, 455  
 Beswick R. J., Pedlar A., Mundell C. G., Gallimore J. F., 2001, *MNRAS*, **325**, 151  
 Blanchet L., 2006, *Living Reviews in Relativity*, **9**, 4

Blumenthal G. R., Faber S. M., Primack J. R., Rees M. J., 1984, *Nature*, **311**, 517  
 Bortolas E., Franchini A., Bonetti M., Sesana A., 2021, *ApJ*, **918**, L15  
 Brem P., Amaro-Seoane P., Spurzem R., 2013, *MNRAS*, **434**, 2999  
 Campanelli M., Lousto C. O., Zlochower Y., Merritt D., 2007, *Phys. Rev. Lett.*, **98**, 231102  
 Carter C., Karovska M., Jerius D., Glotfelty K., Beikman S., 2003, in Payne H. E., Jedrzejewski R. I., Hook R. N., eds, Astronomical Society of the Pacific Conference Series Vol. 295, Astronomical Data Analysis Software and Systems XII. p. 477  
 Choi D.-I., Kelly B. J., Boggs W. D., Baker J. G., Centrella J., van Meter J., 2007, *Phys. Rev. D*, **76**, 104026  
 Cuadra J., Armitage P. J., Alexander R. D., Begelman M. C., 2009, *MNRAS*, **393**, 1423  
 Dehnen W., 1993, *MNRAS*, **265**, 250  
 Dobrycheva D. V., Vavilova I. B., Melnyk O. V., Elyiv A. A., 2018, *Kinematics and Physics of Celestial Bodies*, **34**, 290  
 Engel H., et al., 2010, *A&A*, **524**, A56  
 Fabbiano G., Paggi A., Karovska M., Elvis M., Nardini E., Wang J., 2020, *ApJ*, **902**, 49  
 Ferrarese L., Merritt D., 2000, *ApJ*, **539**, L9  
 Fiestas J., Porth O., Berczik P., Spurzem R., 2012, *MNRAS*, **419**, 57  
 Freeman P., Doe S., Siemiginowska A., 2001, in Starck J.-L., Murtagh F. D., eds, Proc. SPIE Vol. 4477, Astronomical Data Analysis. pp 76–87 ([arXiv:astro-ph/0108426](https://arxiv.org/abs/astro-ph/0108426)), doi:10.1117/12.447161  
 Fruscione A., et al., 2006, in Proc. SPIE. p. 62701V, doi:10.1117/12.671760  
 Fyhrie A., Glenn J., Rangwala N., Wheeler J., Beck S., Bally J., 2021, *ApJ*, **922**, 208  
 Gallimore J. F., Beswick R., 2004, *AJ*, **127**, 239  
 Gaskin J. A., et al., 2019, *Journal of Astronomical Telescopes, Instruments, and Systems*, **5**, 021001  
 Gerssen J., van der Marel R. P., Axon D., Mihos J. C., Hernquist L., Barnes J. E., 2004, *AJ*, **127**, 75  
 González J. A., Hannam M., Spherhake U., Brüggemann B., Husa S., 2007, *Phys. Rev. Lett.*, **98**, 231101  
 Gröbner M., Ishibashi W., Tiwari S., Haney M., Jetzer P., 2020, *A&A*, **638**, A119  
 Haardt F., Maraschi L., 1991, *ApJ*, **380**, L51  
 Haardt F., Maraschi L., 1993, *ApJ*, **413**, 507  
 Haehnelt M. G., 1994, in Courvoisier T., Blecha A., eds, IAU Symposium Vol. 159, Multi-Wavelength Continuum Emission of AGN. p. 279  
 Hagiwara Y., Diamond P. J., Miyoshi M., 2002, *A&A*, **383**, 65  
 Hagiwara Y., Diamond P. J., Miyoshi M., 2003, *A&A*, **400**, 457  
 Hagiwara Y., Baan W. A., Klöckner H.-R., 2011, *AJ*, **142**, 17  
 Hénon M. H., 1971, *Ap&SS*, **14**, 151  
 Hernquist L., 1990, *ApJ*, **356**, 359  
 Hobbs G., 2013, *Classical and Quantum Gravity*, **30**, 224007  
 Husemann B., Heidt J., De Rosa A., Vignali C., Bianchi S., Bogdanović T., Komossa S., Paragi Z., 2020, *A&A*, **639**, A117  
 Iono D., et al., 2007, *ApJ*, **659**, 283  
 Jaffe W., 1983, *MNRAS*, **202**, 995  
 Kauffmann G., Colberg J. M., Diaferio A., White S. D. M., 1999, *MNRAS*, **303**, 188  
 Khan F. M., Fiacconi D., Mayer L., Berczik P., Just A., 2016, *ApJ*, **828**, 73  
 Khan F. M., Berczik P., Just A., 2018a, *A&A*, **615**, A71  
 Khan F. M., Capelo P. R., Mayer L., Berczik P., 2018b, *ApJ*, **868**, 97  
 Kidder L. E., 1995, *Phys. Rev. D*, **52**, 821  
 Kollatschny W., Weilbacher P. M., Ochmann M. W., Chelouche D., Monreal-Ibero A., Bacon R., Contini T., 2020, *A&A*, **633**, A79  
 Komossa S., Burwitz V., Hasinger G., Predehl P., Kaastra J. S., Ikebe Y., 2003, *ApJ*, **582**, L15  
 Kompaniets O. V., Vasylenko A. A., 2020, *Astrophysics*, **63**, 307  
 Kormendy J., Ho L. C., 2013, *ARA&A*, **51**, 511  
 Kormendy J., Richstone D., 1995, *ARA&A*, **33**, 581  
 Kramer M., Champion D. J., 2013, *Classical and Quantum Gravity*, **30**, 224009  
 Kupi G., Amaro-Seoane P., Spurzem R., 2006, *MNRAS*, **371**, L45  
 Le Tiec A., 2014, *International Journal of Modern Physics D*, **23**, 1430022

- Li S., Liu F. K., Berczik P., Chen X., Spurzem R., 2012, *ApJ*, **748**, 65
- Lodato G., Nayakshin S., King A. R., Pringle J. E., 2009, *MNRAS*, **398**, 1392
- Manchester R. N., IPTA 2013, *Classical and Quantum Gravity*, **30**, 224010
- Matt G., Perola G. C., Piro L., 1991, *A&A*, **247**, 25
- Maureira-Fredes C., Goicovic F. G., Amaro-Seoane P., Sesana A., 2018, *MNRAS*, **478**, 1726
- Medling A. M., Ammons S. M., Max C. E., Davies R. I., Engel H., Canalizo G., 2011, *ApJ*, **743**, 32
- Menci N., Cavaliere A., Fontana A., Giallongo E., Poli F., 2002, *ApJ*, **575**, 18
- Merritt D., 2001, *ApJ*, **556**, 245
- Merritt D., Ferrarese L., 2001, *MNRAS*, **320**, L30
- Milosavljević M., Merritt D., 2003a, *ApJ*, **596**, 860
- Milosavljević M., Merritt D., 2003b, in Centrella J. M., ed., *American Institute of Physics Conference Series Vol. 686, The Astrophysics of Gravitational Wave Sources*. pp 201–210 ([arXiv:astro-ph/0212270](https://arxiv.org/abs/astro-ph/0212270)), [doi:10.1063/1.1629432](https://doi.org/10.1063/1.1629432)
- Müller-Sánchez F., Nevin R., Comerford J. M., Davies R. I., Privon G. C., Treister E., 2018, *Nature*, **556**, 345
- Mushotzky R. F., Done C., Pounds K. A., 1993, *ARA&A*, **31**, 717
- Nandra K., 2006, *MNRAS*, **368**, L62
- Nandra K., et al., 2013, arXiv e-prints, p. [arXiv:1306.2307](https://arxiv.org/abs/1306.2307)
- Nardini E., 2017, *MNRAS*, **471**, 3483
- Nasim I., Gualandris A., Read J., Dehnen W., Delorme M., Antonini F., 2020, *MNRAS*, **497**, 739
- Pasquali A., de Grijs R., Gallagher J. S., 2003, *MNRAS*, **345**, 161
- Perets H. B., Hopman C., Alexander T., 2007, *ApJ*, **656**, 709
- Peters P. C., 1964a, PhD thesis, California Institute of Technology
- Peters P. C., 1964b, *Physical Review*, **136**, 1224
- Peters P. C., Mathews J., 1963, *Physical Review*, **131**, 435
- Pignata G., et al., 2010, Central Bureau Electronic Telegrams, **2591**
- Plummer H. C., 1911, *MNRAS*, **71**, 460
- Preto M., Berentzen I., Berczik P., Spurzem R., 2011, *Astrophys. J., Lett.*, **732**, L26
- Puccetti S., et al., 2016, *A&A*, **585**, A157
- Quinlan G. D., 1996, *New Astron.*, **1**, 35
- Ransom S., et al., 2019, in *Bulletin of the American Astronomical Society*. p. 195 ([arXiv:1908.05356](https://arxiv.org/abs/1908.05356))
- Rantala A., Pihajoki P., Johansson P. H., Naab T., Lahén N., Sawala T., 2017, *ApJ*, **840**, 53
- Reisswig C., Husa S., Rezzolla L., Dorband E. N., Pollney D., Seiler J., 2009, *Phys. Rev. D*, **80**, 124026
- Ricci C., Ueda Y., Ichikawa K., Paltani S., Boissay R., Gandhi P., Stalewski M., Awaki H., 2014, *A&A*, **567**, A142
- Richstone D., et al., 1998, *Nature*, **385**, A14
- Rybicki G. B., Lightman A. P., 1979, *Radiative processes in astrophysics*. A Wiley-Interscience Publication, New York
- Sanders D. B., Mazzarella J. M., Kim D. C., Surace J. A., Soifer B. T., 2003, *AJ*, **126**, 1607
- Sobolenko M., Berczik P., Spurzem R., 2016, in Meiron Y., Li S., Liu F. K., Spurzem R., eds, *Proceedings of the International Astronomical Union, IAU Symposium Vol. 312, Star Clusters and Black Holes in Galaxies across Cosmic Time*. pp 105–108, [doi:10.1017/S1743921315007620](https://doi.org/10.1017/S1743921315007620)
- Sobolenko M., Berczik P., Spurzem R., Kupi G., 2017, *Kinematics and Physics of Celestial Bodies*, **33**, 21
- Sobolenko M., Berczik P., Spurzem R., 2021, *A&A*, **652**, A134 (S21)
- The Lynx Team 2018, arXiv e-prints, p. [arXiv:1809.09642](https://arxiv.org/abs/1809.09642)
- Treister E., et al., 2020, *ApJ*, **890**, 149
- Tremaine S., et al., 2002, *ApJ*, **574**, 740
- Vasylenko A. A., 2018, *Ap&SS*, **363**, 228
- Vavilova I. B., et al., 2015, *Dark matter: Observational manifestation and experimental searches*. Kyiv, Akadempriodyka, [doi:10.15407/akadempriodyka.287.356](https://doi.org/10.15407/akadempriodyka.287.356)
- Wang L., Berczik P., Spurzem R., Kouwenhoven M. B. N., 2014a, *ApJ*, **780**, 164
- Wang J., et al., 2014b, *ApJ*, **781**, 55
- White S. D. M., Rees M. J., 1978, *MNRAS*, **183**, 341
- Wise M., 1997, *Chandra News*, **5**, 22
- Wright E. L., 2006, *PASP*, **118**, 1711
- Wyithe J. S. B., Loeb A., 2003, *ApJ*, **590**, 691
- Yu Q., 2002, *MNRAS*, **331**, 935
- Zhong S., Berczik P., Spurzem R., 2014, *ApJ*, **792**, 137
- Zoldan A., De Lucia G., Xie L., Fontanot F., Hirschmann M., 2019, *MNRAS*, **487**, 5649

This paper has been typeset from a  $\text{\TeX}/\text{\LaTeX}$  file prepared by the author.